Automatic Resonance Tuning in Wireless Power Transmission System Utilizing Flexible Coil

Guoyuan Cen, Congling Wang, Ping Yang, Amr S. Zalhaf, and Yang Han, *Senior Member, IEEE*

***Abstract*—This article focuses on examining the transmission characteristics of a wireless power transfer (WPT) system that employs flexible coils in folded configuration. The detuning phenomenon resulting from variations in the shape of flexible coil is explored, and a compensation method is proposed. The analysis of dual-coil system operating in LCC-S configuration is conducted through theoretical analysis and numerical simulations to assess the effects of detuning on the transmission properties of system. The findings indicate that the equivalent inductance of coil is diminished by deformation, leading to a degradation of the transmission characteristics as the deformation angle decreases. This deterioration causes the WPT system to transition into the detuned state, thereby reducing the output power and efficiency. To mitigate the impact of flexible coil deformation, an automatic resonance tuning circuit is designed based on the switched capacitance compensation. Adaptive reactance compensation technique is used for the receiver and equivalent capacitance compensation technique is used for the transmitter. Furthermore, automatic resonance tuning circuits are created by integrating a phase comparator and an over-zero detection circuit on the transmitter side. The capacitance value is continuously compensated by adjusting the control signal of the switching tube, ensuring the phase synchronization between the input current and voltage. Finally, the hardware circuit has been designed and the experimental platform has been built. The detuning of 30, 60, 90, 120, and 150 folding angles, as well as the output of the circuit after compensation, have been analyzed, respectively. The experimental results demonstrate that the system can effectively compensate for the effect of coil distortion and improve the output efficiency by at least 20%.**

***Index Terms*—Detuned state, detuning compensation, dynamic tuning feedback, flexible coil.**

I. INTRODUCTION

THE limitations of rigid coupling mechanisms have become apparent as wireless energy transmission technology advances. These rigid structures cannot deform, constraining wireless energy transmission applications where the target object has a heterogeneous surface or active motion [1], [2], [3]. The flexible coupling mechanism has been introduced as a solution to address these challenges. This flexible approach can be arbitrarily deformed, enabling it to adapt to a variety of nonplanar, shaped structures [4], [5]. Flexible coils hold significant potential for wireless charging applications in foldable and rollable electronic product [6]. Additionally, flexible coils can be embedded within foldable or rollable wearable devices, allowing for excellent conformity to the contours of the human body [7], [8]. Nonimplantable flexible wearable devices such as smart watches and smart human information monitoring bracelets can support higher charging power. In the realm of medical implantable devices [9], [10], flexible coils can also be used in pacemakers and other devices that need to adapt to various body curves and movements. However, considering the sensitivity and fragility of vital organs in the human body, the power of implantable devices should not be too large. Flexible coils are designed for robotic joints, conforming to the joints' shapes and being fixed internally within the robot. The flexibility and compliance of these flexible coils are then leveraged to achieve stable wireless power and signal transmission during joint movement [11]. In the aerospace sector, flexible coils can be applied to the surfaces of aircraft bodies and doors, which require adaptation to curves and deformations, thereby supporting wireless communication and wireless charging functionalities [12].

The wireless power transfer operates on the principle of electromagnetic induction, where resonance technology is incorporated to maximize energy transfer by achieving magnetic coupling resonance between the coil and capacitor [13], [14]. Ideally, the system should operate at the resonance frequency point [15]. However, in practical scenarios, the resonance frequency may deviate [16]. This deviation can be attributed to various factors, such as the presence of parasitic capacitance and inductance within the circuit itself, as well as changes in the coil and capacitor values caused by external environmental factors and prolonged operation [17]. The flexible coupling mechanism is inherently more prone to misalignment. Furthermore, the resonance frequency is influenced by the material properties and parasitic parameters inherent to the coupling mechanisms [18], [19], [20]. As a result of bending or folding, deformation of the flexible coupling mechanism, induces changes in its inductance. This phenomenon raises the possibility of the system transitioning into a detuned state, resulting in impeding the functionality of the wireless energy transfer system [21].

While the flexible coupling mechanism offers the advantage of adaptability to various nonplanar structures and enables versatile energy transfer within the system, the performance of WPT systems utilizing flexible coils is susceptible to factors like coil curvature, resonance frequency variations, and power transfer efficiency [22], [23], [24]. In [5], the energy transfer efficiency

---

Received 17 April 2024; revised 10 July 2024 and 14 August 2024; accepted 22 August 2024. Date of publication 29 August 2024; date of current version 7 October 2024. Recommended for publication by Associate Editor M. Ponce-Silva. *(Corresponding author: Yang Han.)*

The authors are with the School of Mechanical and Electrical Engineering University of Electronic Science and Technology of China, Chengdu, Sichuan 611731, China (e-mail: 202222040404@std.uestc.edu.cn; wangcl12@uestc.edu.cn; ping@uestc.edu.cn; amr.zalhaf@uestc.edu.cn; hanyang@uestc.edu.cn).

Color versions of one or more figures in this article are available at https://doi.org/10.1109/TPEL.2024.3450545.

Digital Object Identifier 10.1109/TPEL.2024.3450545

TABLE I
COMPARISON TABLE OF TUNING METHODS

Methods	Specificities	Advantages	Disadvantages
Equivalent capacitive Compensation [32], [33]	The tuning function is realized by controlling the switching tube on and off to change the equivalent capacitance size.	1.Dynamic resonant frequency offset compensation 2.Adjusts for coil deformation frequency shift. 3.Simple, no extra components needed.	1.Cannot compensate for power imbalances from load changes. 2.Requires duty cycle control of switching tubes.
Auxiliary Measuring Coil Compensation Method [34]	Receiver induced voltage phase measured directly; resonance condition determined by calculating phase difference between induced voltage and receiver current.	1.Detects load changes in real-time. 2.Directly measures system resonance 3.Accurately identifies resonance.	1.Adding additional measuring coils and their detection circuits 2.Challenging to position and configure. 3.Limited for dynamic wireless systems.
Parameter identification tuning [30]	Resonant circuit parameters identified from coil current RMS. Adjusting frequency and active rectifier phase minimizes reactance on both sides.	1.Identifying system or device key parameters. 2.Compensation can be customized for specific system characteristics.	1.Parameter identification affected by noise. 2.Time-varying system parameters need periodic calibration and adjustment.
Phase control method. [11], [29], [31]	The phase control method optimizes power transfer efficiency by detecting the voltage-current phase difference between transmitter and receiver, and dynamically adjusting the phase control circuit through feedback control.	1.Optimizes power/energy transfer efficiency. 2.Suitable for bidirectional or multi-device charging. 3.Compensates for power imbalance from changing conditions.	1.Limited parameter change tolerance. 2.Incomplete compensation for coil parameter changes. 3.May reduce overall efficiency.

experiences a notable decline as the resonance frequency shifts due to the flexible coil surpassing the critical curvature threshold. In [25], the utilization of flexible bent relay coils within wearable textiles was emphasized for its capability to significantly extend the range of wireless energy transmission. Nonetheless, as the curvature of the coil increases, there is a notable decline in the power of WPT [26]. The deformation of a flexible coil leads to a nonlinear decrease in self-inductance and mutual inductance as the bending radius decreases linearly. Moreover, decreasing the bending radius reduces transmission efficiency and shifts the resonant frequency to a higher range, causing system detuning [27], [28].

To solve the problem of detuning of flexible coils, the method of adjusting the equivalent load impedance by manipulating the phase shift and output voltage of an active rectifier was presented in [29]. This method aims to counteract the reactance induced by detuning on the receiver coil side, ultimately achieving maximum transmission efficiency. In [30], an impedance tuning method based on parameter identification without a phase detection circuit and auxiliary measurement coil was proposed. This technique ensures that the operating frequency of the inverter closely tracks the resonance frequency, optimizing system performance. In [31], proposes an adaptive detuning correction circuit and corresponding parameter design rules to ensure that the WPT system always operates in a resonant state with optimal power transfer capability. A method of using synchronous series compensators instead of shunt capacitors in a receiver to improve tuning accuracy was presented in [11]. The switching tube and capacitor tuning compensation method has been developed, which uses the turn-ON and turn-OFF times of the switching transistor to charge and discharge a fixed capacitor, providing an equivalent capacitance that compensates for detuned circuits [32], [33]. Active single-phase rectifiers with auxiliary measuring coils and controllers have been developed to determine the resonance conditions by calculating the phase of the induced voltage and the received current [34]. The comparison table of various tuning methods is shown in Table I.

In this article, a square flexible printed coil is selected as the coupling mechanism for energy transmission. Based on the dual-coil system, the detuned state of the system is analyzed theoretically and numerically in the hybrid LCC-S topology, and circuit simulation is performed. The results show that the deformation of the coil structure will reduce its equivalent inductance. The study of the transmission characteristics of the flexible coil in the folded state shows that the resonant frequency of the system is shifted, and the frequency shift increases with the increase of the deformation angle. To address this problem, an automatic resonance tuning circuit based on LCC-S is designed. The advantage of this design is that when the flexible coil is deformed and causes detuning, the continuity of the capacitance value can be achieved using only one capacitor. Feedback can be completely implemented by analog components, thus avoiding the necessity of digital sampling. No digital sampling, ADC/DAC and microcontroller are required. The phase difference can be swiftly detected. The system can quickly restore resonance by adjusting the equivalent capacitance size. Phase consistency can be maintained without wireless communication, avoiding information loss caused by high-frequency switching and redundant algorithm control. In addition, the system does not need to add measurement coils or pretrain complex mathematical models. Simulation and experimental results show that at the three folding angles of 30°, 60°, and 90°, the efficiency with compensation is 20% higher than that without compensation.

The rest of this article is organized as follows. Section II analyzes the effect of coil folding angle on coil inductance and the detuning phenomenon caused by coil deformation in the LCC-S topology system. Section III presents an automatic detuning compensation method tailored to reduce the detuning effects associated with flexible coils, which is then verified by simulation. Section IV elaborates on the physical circuit design and experimental validation of the system, affirming the accuracy of the simulation results. Finally, Section V offers a comprehensive summary of the research findings.

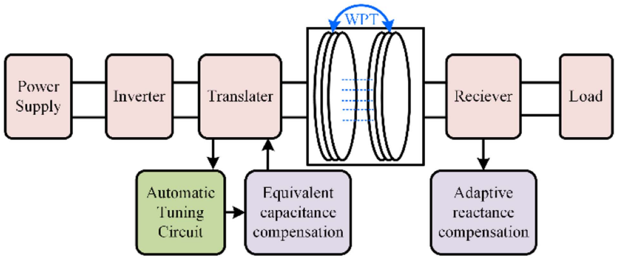

Fig. 1. Structural sketch of the automatic tuning system.

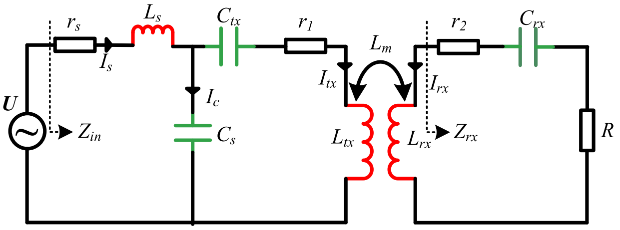

Fig. 2. Topology circuit structure of LCC-S.

II. TWO-COIL COUPLING TOPOLOGY DETUNING ANALYSIS

In WPT systems, a wide range of topologies are utilized, with the dual-coil structure being the prevailing choice. Moreover, building upon the dual-coil topology, numerous high-performance variants have been developed. Examples of these hybrid configurations include the S-SP and LCC-S [35], [36]. During the wireless charging process, the deformation of the coil winding will cause the geometric center to shift, thereby reducing the coupling coefficient, while the load fluctuation will cause the current in the transmitter coil to change. The output current of the *LCC* topology is not affected by changes in the secondary and primary inductances. Furthermore, the *LCC* topology is employed to stabilize the resonant frequency. Consequently, the LCC-S topology has been selected for use in this article. The automatic tuning system, shown in Fig. 1, integrates equivalent capacitance and adaptive compensation in the LCC-S circuit, improving performance. This section analyzes the impact of coil deformation on the LCC-S circuit.

A. Analysis of Detuned State of LCC-S Hybrid Topology

The influence of coil deformation on the system efficiency and power will be comprehensively examined in this section. To achieve this, a circuit analysis of the LCC-S topology structure will be conducted. As shown in Fig. 2, the conventional LCC-S topology circuit diagram will be used for analysis. Where U is the system input ac power supply, Z_{in} is the equivalent input impedance of the system input, C_{tx} is the compensation capacitance at the transmitter side, r_1 is the parasitic resistance in series at the transmitter side, I_{tx} is the transmitter current at the transmitter side, L_{tx} is the equivalent inductance of the transmitter coil at the transmitter side, L_{rx} is the equivalent inductance of the receiver coil at the receiver side, L_m is the mutual inductance between the transmitter coil and the receiver coil, I_{rx} is the receiver current at the receiver side, r_2 is the parasitic resistance in series at the receiver side, C_{rx} is the compensation capacitance at the receiver side, R is the load of the receiver side of the system, I_s the system input current, L_S is the emitter compensation inductor, r_s is the parasitic resistance of the compensation inductor, C_s is the emitter compensation shunt capacitor, and I_c is the current flowing through the shunt compensation capacitor.

The impedance Z_{rx} at the receiver can be derived from the receiver as follows:

$$Z_{rx} = r_2 + R + j\left(\omega L_{rx} - \frac{1}{\omega C_{rx}}\right). \tag{1}$$

The reflected impedance Z_{rf} of the reflection to the transmitter can be obtained as follows:

$$Z_{rf} = \frac{\omega^2 {L_m}^2}{r_2 + R + j\left(\omega L_{rx} - \frac{1}{\omega C_{rx}}\right)}. \tag{2}$$

The input impedance of the system Z_{in} can be obtained from the transmit impedance as follows:

$$Z_{\text{in}} = \frac{1}{\frac{1}{Z_{rf}+r_1+j\omega L_{tx}+\frac{1}{j\omega C_{tx}}} + j\omega C_S} + j\omega L_S + r_S. \tag{3}$$

The system input current I_S can be obtained as follows:

$$I_S = \frac{U}{r_S + j\omega L_S + \frac{\frac{1}{j\omega C_S}\left(\frac{1}{j\omega C_{tx}}+j\omega L_{tx}+r_1+Z_{rf}\right)}{\frac{1}{j\omega C_S}+\frac{1}{j\omega C_{tx}}+j\omega L_{tx}+r_1+Z_{rf}}}. \tag{4}$$

By Kirchhoff's current law, the transmitter current I_{tx} can be obtained as follows:

$$I_{tx} = I_S \frac{\frac{1}{j\omega C_S}}{\frac{1}{j\omega C_S} + \frac{1}{j\omega C_{tx}} + j\omega L_{tx} + r_1 + Z_{rf}}. \tag{5}$$

Through the theory of circuit mutual inductance, the current at the receiver I_{rx} can be obtained as follows:

$$I_{rx} = \frac{j\omega L_m I_{tx}}{r_2 + R + j\left(\omega L_{rx} - \frac{1}{\omega C_{rx}}\right)}. \tag{6}$$

From the conjugate complex expression for the transmit current ${I_{tx}}^*$ and the receive current ${I_{rx}}^*$, the system efficiency can be deduced as follows:

$$\begin{cases} P_{\text{in}} = I_{tx} I_{tx}^* Z_{\text{in}} = \frac{U^2 Z_C}{Z_B Z_C - Z_A^2} \\ P_{\text{out}} = I_{rx} I_{rx}^* R = \frac{\omega^2 L_M^2 Z_A^2 U_S^2 R}{[Z_2(Z_B Z_C - Z_A^2)]^2} \\ \eta = \frac{P_{\text{out}}}{P_{\text{in}}} = \frac{\omega^2 L_M^2 Z_A^2 R}{Z_C Z_2^2 (Z_B Z_C - Z_A^2)} \end{cases} \tag{7}$$

where

$$\begin{cases} Z_A = -\frac{1}{\mathrm{j}\omega C_{\mathrm{rx}}} \\ Z_B = \mathrm{j}\omega L_S + \frac{1}{j\omega C_s} \\ Z_C = r_1 + j\omega L_{tx} + \frac{1}{j\omega C_{tx}} + \frac{1}{j\omega C_s} + Z_{rf} \\ Z_2 = r_2 + R + j\omega L_{tx} + \frac{1}{j\omega C_{rx}}. \end{cases}$$

From (3), when the inductance of the coil changes, the input impedance of the system will be altered, resulting in the formation of a capacitive or inductive circuit. Coil deformation, regardless of which end, leads to a reduction in system transmission efficiency, primarily due to the decrease in coil inductance,

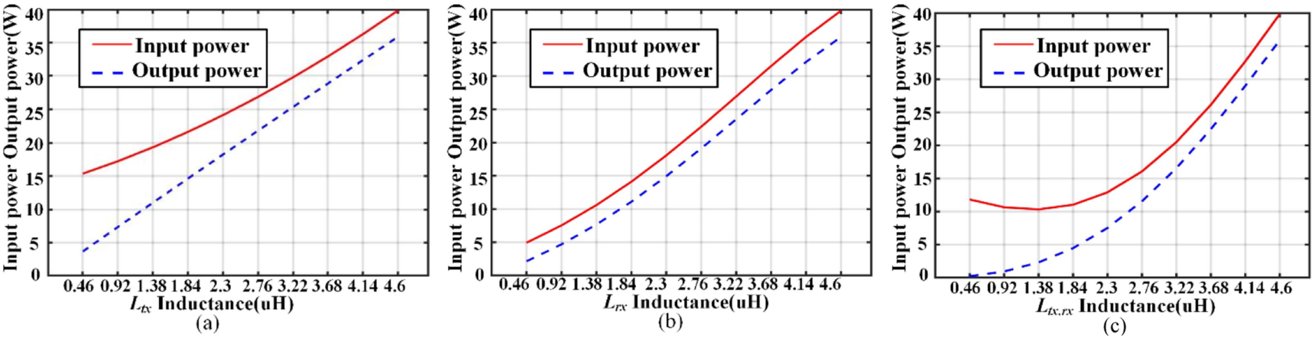

(a) (b) (c)

Fig. 3. Curves of Input and output power change caused by coil deformation. (a) Transmitter coil change. (b) Receiver coil change. (c) Transmitter and receiver coils change at the same time.

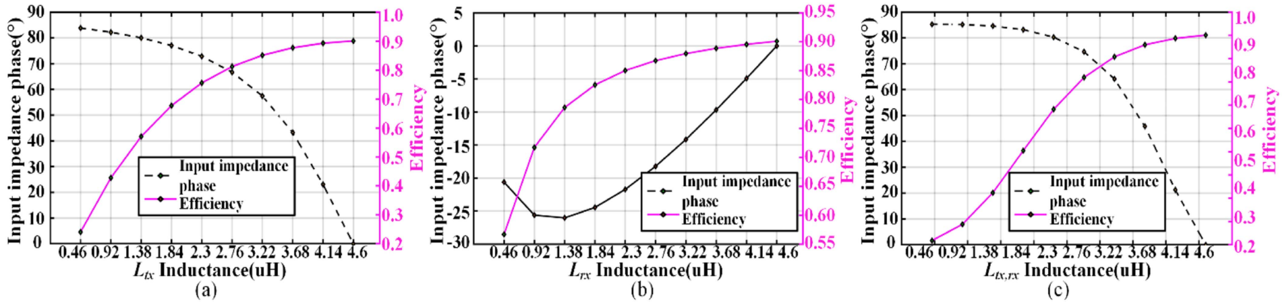

(a) (b) (c)

Fig. 4. Curve of efficiency and impedance change caused by coil deformation. (a) Transmitter coil change. (b) Receiver coil change. (c) Transmitter and receiver coils change at the same time.

TABLE II
SIMULATION PARAMETER TABLE

Symbol	Parameter	Value	Unit
L_s	Compensating inductance of transmitter	2.3	μH
C_s	Compensating capacitor of transmitter	44	nF
C_{tx}	Compensating capacitor of transmitter	44	nF
C_{rx}	Compensating capacitor of receiver	22	nF
L_{tx}	Transmitter coil inductance	4.6	μH
L_{rx}	Receiver coil inductance	4.6	μH
L_m	Mutual inductance of transmitter and receiver	2.3	μH
R	Load resistance	15	Ω

causing the transmitter or receiver to operate in a detuned state. According to (7), the system transmission efficiency will be reduced. Numerical analysis was conducted by substituting Table II parameters into relevant equations. The inductance of the coil is affected by the folding angle, so the impact of different folding angles on circuit detuning was simulated by varying the inductance value.

When the transmitting coil is deformed while the receiving coil remains unchanged, the impact on system transmission characteristics is first considered. In this scenario, the transmitting coil starts to fold from the planar state, and the folding angle gradually increases, causing the inductance of the transmitting coil to decrease from the initial value of 4.6 to 0.46 μH. Numerical analyses have been performed based on (3) and (7) to obtain the corresponding input and output power curves, the system efficiency curve, and the input impedance phase curve. As shown in Fig. 3(a), system input and output power are maximized when the transmitting coil is in the planar, undeformed state, and decrease as the coil is deformed. As shown in Fig. 4(a), system transmission efficiency is maximized when transmitting coil is in initial, undeformed state, and decreases with coil deformation. Input impedance phase shifts from 0° to 84.4°, implying deformation reduces coil inductance, causing system to become inductive, with voltage phase leading current phase. In conjunction with the curve in the figure, the wireless transmission system will be detuned when the deformation of the transmitter coil causes the coil inductance to decrease, resulting in a reduction in the output power transmitted to the load, and ultimately a reduction in the system's efficiency.

When the receiving coil undergoes flexible deformation while the transmitting coil remains unchanged, the impact on system transmission characteristics is considered. As shown in Fig. 3(b), when the receiver transitions from its initial state to a deformed state, a decrease in both input and output power is observed. With an appreciable folding angle of the receiver coil, the inductance is significantly reduced, and a declining trend in the overall efficiency of the system is exhibited. Furthermore, as depicted in Fig. 4(b), the input impedance of the system is rendered capacitive following the reduction in the inductance of the receiving coil. As receiving coil deforms, its inductance decreases. This inductance decrease causes overall impedance at receiver to become inductive. When reflected back to transmitter, it forms capacitive input impedance of the system.

Finally, the effect on the transmission characteristics of the system when the transmitting and receiving coils are simultaneously subjected to flexible deformation is considered. In Fig. 4(c), the input impedance is observed to be inductive. This occurs because the impact of the impedance reflected to the transmitter due to the deformation of the receiving coil is minor compared to the impedance change induced by the deformation of the transmitting coil.

In the LCC-S series topology, the deformation of the transmitter coil is identified as the primary factor determining the impedance parameters. Coil deformation causes the input impedance to shift, which ultimately leads to reduced input and output power of the system. The decrease in coil inductance due to deformation results in detuning of the transmitter or receiver side, resulting in a reduction in the transmission efficiency of the system. This efficiency decline is observed to accelerate as the degree of coil deformation increases.

B. Detuning Simulation Analysis

The analysis above reveals that within the LCC-S topology, coil deformation induces a change in coil inductance, leading to detuning of the entire system. As a consequence of this detuning, the input impedance of the system shifts, resulting in its transition into capacitive or inductive state. Maximized system transmission power occurs when the input impedance is purely resistive, indicating a resonant state. The simulations based on the parameters in Table II verify the accuracy of the theoretical and numerical analyses and lay a solid foundation for the subsequent research.

Three flexible deformation cases are analyzed in simulation. As described in the previous section, the folding of the coil is simulated by applying a stepwise reduction in the inductance. The flexible deformation of the transmitting coil was analyzed while keeping the receiving coil unchanged. Transmitting coil inductance was varied from 4.6 to 0.46 μH, increasing by 0.46 μH at each step. Effect of varying receiver coil inductance from 4.6 to 0.46 μH, while keeping transmitter coil unchanged, was then studied. Finally, the effect of simultaneous flexible deformation of transmitter and receiver coils was examined. Inductances of both coils transitioned from initial values to 0.46 μH, with increments of 0.46 μH at each step.

In Fig. 5(a), the input current amplitude increases as the inductance of the transmitter coil decreases due to coil deformation. The decrease in the real component of the input current indicates an increase in reactive power and a decrease in active power in the detuned circuit. Moreover, the input current lags behind the input voltage, indicating the inductive characteristics of circuit at that time. In Fig. 5(b), the input current magnitude decreases as the inductance of the receiving coil decreases due to coil deformation. Additionally, the input current leads the voltage in phase, indicating a capacitive characteristic of the circuit. In Fig. 5(c), when both the transmitter and receiver coils deform, the curve characteristics closely resemble those observed when only the transmitting coil is deformed. This result illustrates once again that the deformation of the transmitting coil has a greater impact compared to the deformation of the receiving coil. Therefore, only the deformation of the transmitting coil was considered in the experiment.

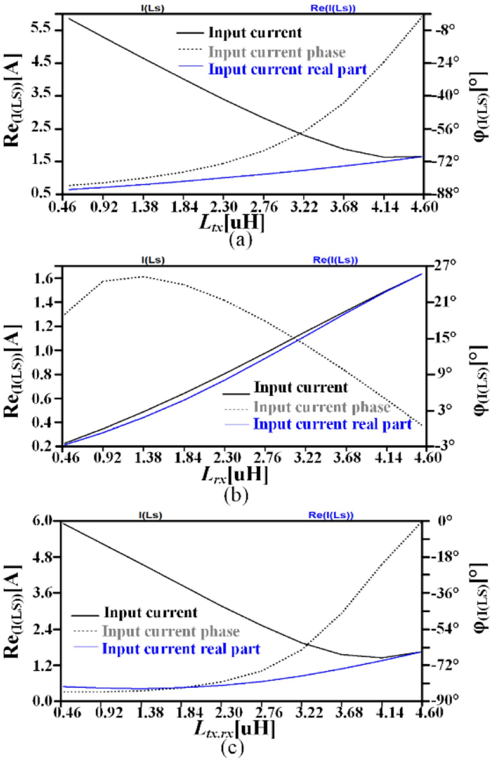

Fig. 5. Transmission characteristic curves for LCC-S series topology coil deformation. (a) Transmitter coil change. (b) Receiver coil change. (c) Transmitter and receiver coils change at the same time.

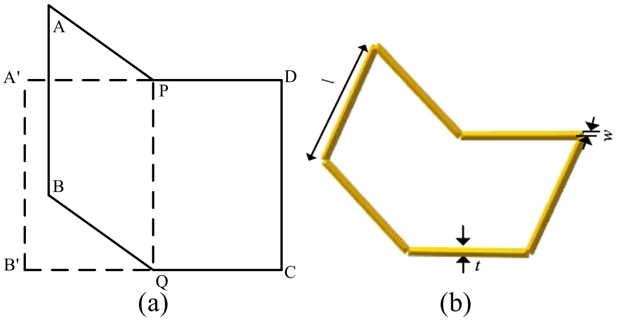

Fig. 6. (a) Schematic of coil folding plane. (b) Schematic of coil folding 3-D.

C. Single Gate Coil Folding Analysis

The equivalent inductance of FPC coil is observed to be affected by structural parameters including inner/outer diameters, turn spacing, and number of turns, which are found to influence inductance [37], [38]. This section seeks to analyze the inductance variation of an FPC coil folded in half at the center, based on a simplified single-turn closed coil model.

Fig. 6 is a schematic diagram of a single-turn square coil, assuming that the coil length is $l = 10$ mm, the single turn coil line width is $w = 0.1$ mm, the thickness of the single turn coil is $t = 0.035$ μm, and the coil is folded from the middle. According to the total inductance formula, the total inductance of the single-turn square folded coil can be obtained as follows:

$$L = L_{AB} + L_{CD} + L_{BQC} + L_{APD} - M_{AB-CD} - M_{CD-AB} - M_{BQC-APD} - M_{APD-BQC} \quad (8)$$

where L is the total inductance of the single-turn square folded coil, L_{AB} and L_{CD} are the self-inductance of the two segments at the unbent end and $L_{AB} = L_{CD}$, $M_{AB\text{-}CD}$ and $M_{CD\text{-}AB}$ are the mutual inductance between the two segments at the unbent end, because the two segments are parallel and of equal length, so $M_{AB\text{-}CD} = M_{CD\text{-}AB}$, the L_{BQC} and L_{APD} are the inductance of the two segments at the bent end, and $L_{BQC} = L_{APD}$, $M_{BQC\text{-}APD}$ and $M_{APD\text{-}BQC}$ are the mutual inductance between the two segments at the bent end, and similarly, $M_{BQC\text{-}APD} = M_{APD\text{-}BQC}$.

The total inductance of single turn square folded coil reduces to the following:

$$L = 2L_{AB} + 2L_{BQC} - 2M_{AB-CD} - 2M_{BQC-APD}. \quad (9)$$

According to Yuan et al. [39], the single segment unbent coil inductance is calculated as follows:

$$L_{AB} = \frac{\mu_0 l}{2\pi}\left\{\ln\left(\frac{2l}{w+t}\right) + \frac{1}{2}\right\} \quad (10)$$

where $\mu = 4\pi \times 10^{-7}$Vs/(Am).

The bending section coil inductance is as follows:

$$\begin{aligned} L_{BQC} &= L_{BQ} + L_{QC} - M_{BQ-QC} - M_{QC-BQ} \\ &= 2L_{BQ} - 2M_{BQ-QC} \end{aligned} \quad (11)$$

where the inductance L_{BQ} is ascertained through a comparable computational approach as that detailed in (9), though the length of the constituent line segment is diminished to half the original magnitude.

The mutual inductance between the line segments BQ and QC is $M_{BQ\text{-}QC}$ and the mutual inductance between two equal wires intersecting at a point of angle θ is calculated by the following:

$$M_{BQ-QC} = \frac{\mu_0 l}{2\pi}\cos\theta \tanh^{-1}\left(\frac{1}{1+\sqrt{2(1-\cos\theta)}}\right). \quad (12)$$

The mutual inductance $M_{AB\text{-}CD}$ between lines AB and CD is as follows:

$$\begin{aligned} &M_{AB-CD} \\ &= \frac{\mu_0 l}{2\pi}\left[\ln\left(\frac{l}{d}+\sqrt{1+\left(\frac{l}{d}\right)^2}\right) - \sqrt{1+\left(\frac{l}{d}\right)^2} + \frac{d}{l}\right] \end{aligned} \quad (13)$$

where d denotes the distance between the line segment *AB* and *CD*.

The mutual inductance $M_{BQC\text{-}APD}$ between the curved line segment BQC and APD is as follows:

$$M_{BQC-APD} = 2M_{BQ-AP} - 2M_{BQ-PD}. \quad (14)$$

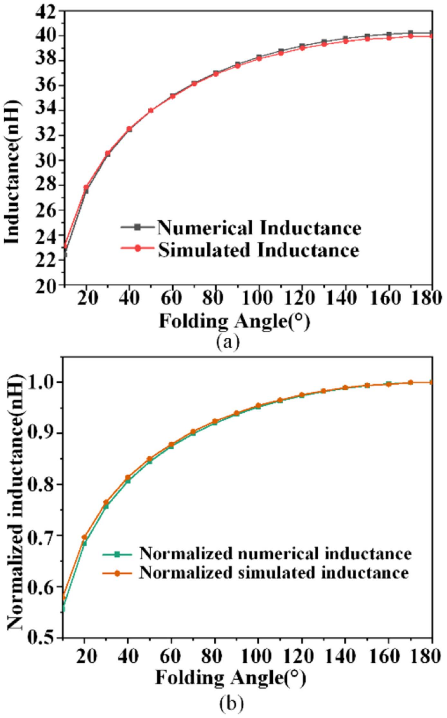

Fig. 7. Folded inductance variation diagram of a single turn square coil. (a) Folded coil inductance value. (b) Folded coil normalized value.

The mutual inductance between lines BQ and PD is calculated as follows:

$$M_{BQ-PD} = 0.1\cos\theta\left[2l\cdot\tanh^{-1}\left(\frac{l}{2(d_1+d_2)}\right) - \Omega\frac{l}{\sin\theta}\right] \quad (15)$$

where

$$\begin{aligned} \Omega &= \tan^{-1}\left(\frac{l^2\cos\theta + (l/2)^2(\sin\theta)^2}{ld_1\sin\theta}\right) \\ &\quad - 2\tan^{-1}\left(\frac{l}{d_2\tan\theta}\right) + \frac{\pi}{2} - \theta \\ d_1 &= \sqrt{l^2 + 2\left(\frac{l}{2}\right)^2(1-\cos\theta)} \\ d_2 &= \sqrt{l^2 + \left(\frac{l}{2}\right)^2}. \end{aligned}$$

According to the above equation, the total inductance L of a single-turn square folded coil can be calculated as a function of the folding angle θ. The results obtained by numerical calculation and simulation are shown in Fig. 7. As shown in Fig. 7(a), inductance of a single-turn square coil decreases as the center is folded, with smaller folding angles corresponding to lower inductance values. Furthermore, as shown in Fig. 7(b), the inductance remains relatively stable, only reducing to around 90% of original value, when folding angle ranges from 180° to 90°. However, the rate of inductance reduction increases significantly when the angle is reduced from 90° to 10°, with

TABLE III
PARAMETERS OF FLEXIBLE COILS

Symbol	Parameter	Value	Unit
w	Single-turn line width	2	mm
s	Turns spacing	1	mm
d_{out}	Outer diameter of coil	90	mm
d_{in}	Coil inner diameter	56	mm
N	Number of turns	6	
L	FPC board edge length	160	mm
H	FPC board thickness	0.2	mm
t	FPC Alignment Copper Thickness	0.07	mm

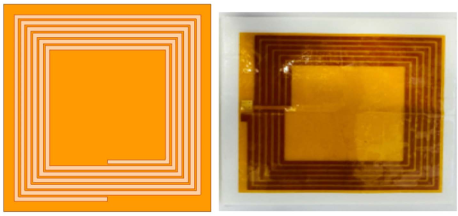

Fig. 8. (a) Model of square coil. (b) Physical picture of square coil.

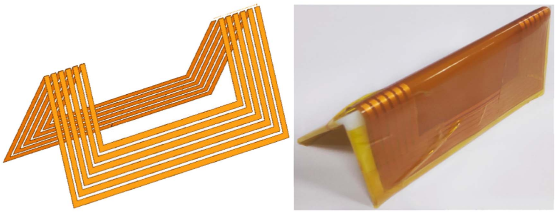

Fig. 9. (a) Folding model of FPC square coil. (b) Picture of FPC square coil folding.

inductance dropping to approximately 55% of original value at a 10° folding angle.

D. Folded Coil Angle Analysis

As discussed in the previous section, the inductance of a single-turn square coil is observed to change when the coil is folded. Furthermore, the inductance of a single-turn coil is typically too small to be effectively utilized as the coupling mechanism in actual wireless transmission systems. To address this, the design often requires the use of coils with more turns and larger sizes to achieve the desired coupling characteristics. The parameters of the determined coil are shown in Table III. The square coil modeling diagram is shown in Fig. 8(a) and the physical diagram is shown in Fig. 8(b).

After determining the coil parameters, the characteristics of coil folding can be considered. As shown in Fig. 9, an FPC square coil folding model was established and the corresponding physical object fabricated. Based on the analysis demonstrating that folding a single-turn square coil reduces its inductance, the present FPC square coil, comprising six turns of differently sized single-turn square coils, is also expected to exhibit a decrease in overall inductance when subjected to folding.

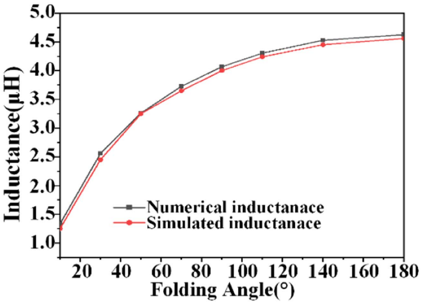

Fig. 10. Diagram of FPC square coil folding simulation inductance and measured inductance.

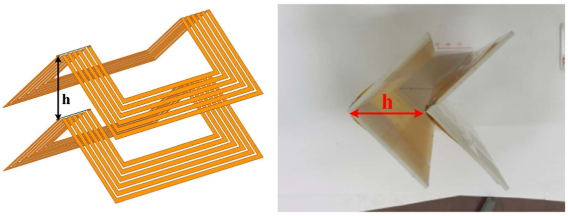

Fig. 11. (a) Folded transmitter–receiver coil simulation model. (b) Physical drawing of folded transmitter-receiver coil.

The inductance characteristics of the folded coil were modeled and simulated using Ansys Electronics software, and subsequently verified through Smith chart measurement using a vector network analyzer. The simulation data is found to agree well with the measured data, as depicted in Fig. 10, and when the folding angle of the FPC square coil is in the range of 180° to 90°, the inductance variation is observed to be small. In the range of 90° to 10° folding angle, the inductance change becomes more pronounced, which is consistent with the trend of the inductance change exhibited by the single-turn square coil under the folding condition.

As shown in Fig. 10, folding the FPC square coil leads to a decrease in the inductance. When the flexible coil was in the flat state, the inductance was 4.56 μH, but as the folding angle increased, the inductance gradually decreased, reaching 1.25 μH at 10 degrees of folding. The inductance decrease leads to the originally resonant wireless energy transmission system becoming detuned, causing a frequency shift. In practical applications, folding is commonly classified into unilateral and bilateral types. This article has selected the more representative bilateral folding configuration for investigation.

In Fig. 11, the transmitter and receiver coils are symmetrically folded, aligning the folding axis of the receiver coil with the centerline of the transmitter coil. The LCC-S circuit is swept and analyzed in the HFSS simulation. For the transmitter coil, a compensation inductor with an inductance value of 2.3 μH and two compensation capacitors with capacitance values of 44 nF each have been added. Additionally, a compensation capacitor with a capacitance value of 22 nF has been added to the receiver coil. The separation distance between the coils (h) has

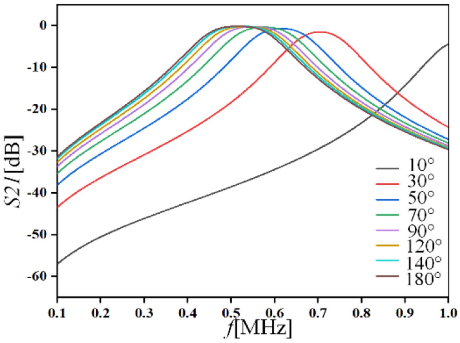

Fig. 12. Sweeping characteristics of transmitter–receiver coils at different folding angles at the same time.

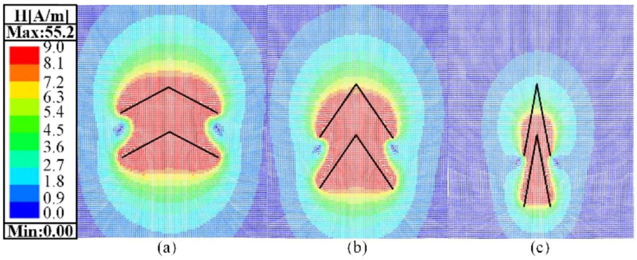

Fig. 13. Magnetic field diagrams for different folding angles. (a) Transmit-receive coil folded 140°. (b) Transmit-receive coil folded 90°. (c) Transmit-receive coil folded 30°.

a significant impact on their coupling coefficient. Assuming $h = 30$ mm in this simulation, it plays a crucial role in determining the efficiency and performance of the coupled coil system.

In Fig. 12, the simultaneous folding of the transmitting and receiving coils within a frequency range of 0.1 to 1 MHz reveals distinctive swept frequency characteristics. The ordinal S21 indicates the ac transmission gain from the transmitter to the receiver in decibels. The graph distinctly portrays that as the folding angles of the two coils decrease, the frequency offset progressively increases. Specifically, the original frequency point of 500 kHz shifts closer toward the 1 MHz frequency point, indicating a consequential impact on the transmission power and efficiency of the wireless energy transmission system.

At an operating frequency of 500 kHz for a high-frequency ac input source, the optimal transmission characteristics are observed when both coils are folded completely at an angle of 180°, maximizing the transmission gain. Conversely, at 500 kHz, the transmission gain is found to decrease due to the reduced folding angle, resulting in less than optimal transmission performance. As shown in Fig. 12, the S21 peaks observed at each folding angle are noted to be very close to each other, demonstrating consistency. Additionally, the frequency shift due to the simultaneous folding of both coils is negligible in the 180° to 90° folding angle range. However, a significant frequency shift is observed in the 90° to 10° folding angle range, which is primarily attributed to the variation of coil inductance at different folding angles.

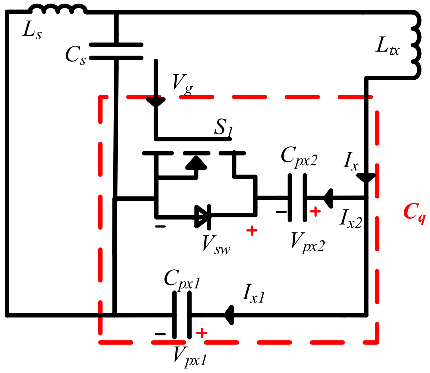

Fig. 14. Circuit diagram of parallel topology for equivalent capacitor compensation.

The simulation results in Fig. 13 for an emitter current of 100 mA highlight the effect of the fold angle change on the magnitude of the magnetic field. At larger folding angles, the magnetic coupling between the two coils is strong, resulting in a wide range of energy transfer between the coils. Conversely, as the folding angle decreases, the magnetic coupling from the transmitter to the receiver gradually weakens, leading to a reduction in the magnetic range. Consequently, power transmission is largely dependent on the magnetic coupling between the two coils. The folding of the FPC coil causes reductions in inductance, leading to frequency shift and detuning in the WPT system.

III. DESIGN OF AUTOMATIC RESONANCE TUNING CIRCUIT

The folding deformation of the FPC square coil leads to a decrease in its inductance, and this decrease becomes more pronounced as the folding angle decreases. As described in the equations in Section II, this reduction in coil inductance causes a shift in the resonant frequency of the WPT system, resulting in a detuned state that degrades the system's transmission performance. This section elucidates an automatic tuning compensation strategy to solve the resonant frequency detuning problem, with the goal of restoring the system to a resonant state through detuning compensation.

A. Equivalent Capacitive Compensation

In a WPT system, the size of the equivalent capacitor can be adjusted by controlling the ON–OFF time of the switching device [32], [33]. Equivalent capacitor compensation techniques are usually categorized into parallel and series topologies. The peak voltage endured by the switching tubes is higher in parallel topology, making it the preferred choice for this design. This parallel topology, depicted in Fig. 14, is utilized at the transmitter of the LCC-S topology circuit to achieve automatic tuning. The modes of operation for equivalent capacitor compensation are shown in Table IV.

MODE ①: During this interval, the switching tube S_1 on working, so the capacitors C_{px1} and C_{px2} shunt the input current I_x.

TABLE IV
OPERATING MODES OF EQUIVALENT CAPACITOR COMPENSATION

	S_1	C_{px1}	C_{px2}
①	On	Charge	Charge
②	Off	Charge	Remain
③	Off	Charge	Charge

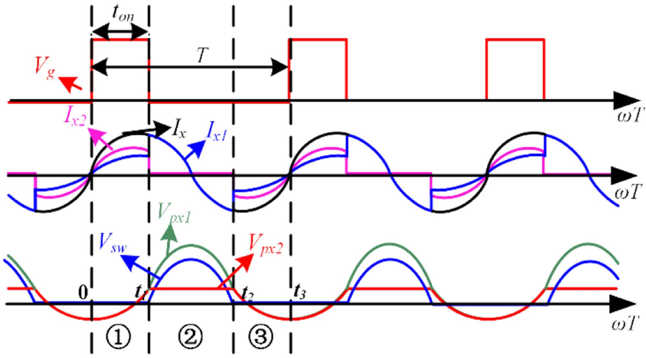

Fig. 15. Main waveforms of equivalent capacitance compensation.

MODE ②: The switching tube S_1 is OFF, at which time the input current I_x is all flowing through the capacitor C_{px}.

MODE ③: The control signal V_g still does not control the switching tube S_1 to be conductive, but the input current I_x is in the reverse direction in this time period, and the switching tube S_1 is flowing the reverse current through the anti-parallel diode D_1.

The circuit analog waveform is shown in Fig. 15. The figure describes in detail the process of current and voltage changes flowing through the compensation capacitor during one switching cycle.

Assuming that the input current I_x waveform is sinusoidal, I_x can be expressed as follows:

$$I_x(t) = \mathrm{I}_m \sin\left(\frac{2\pi}{T} t_{\text{on}}\right) \tag{16}$$

where t_{on} is the time for the control signal V_g to control the switching time, and T is the period of the control signal V_g.

The input current I_x is sinusoidal, but the waveform of V_{px1} is distorted as in Fig. 15, which can be solved for as the fundamental form of V_{px1}

$$\begin{aligned} V_{px1-\text{fund}}(t) &= \frac{2}{T}\int_0^T V_{px1}\cos\left(\frac{2\pi}{T}t\right)dt \\ &= -\frac{TI_m}{2\pi}\left[\frac{1}{C_{px1}} + \left(\frac{1}{C_{px1}+C_{px2}} - \frac{1}{C_{px1}}\right)\right. \\ &\quad \left.\times\left(\frac{2t_{\text{on}}}{T} - \frac{1}{2\pi}\sin\left(\frac{4\pi t_{\text{on}}}{T}\right)\right)\right]. \end{aligned} \tag{17}$$

The equivalent capacitance of the parallel topology can be solved according to (16) and (17), where $D = t_{\text{on}}/T$ is the duty cycle of the control signal V_g. Therefore, C_q is expressed as follows:

$$C_q = \frac{1}{\frac{1}{C_{px1}} + \left(\frac{1}{C_{px1}+C_{p\times2}} - \frac{1}{C_{px1}}\right)\left(2D - \frac{1}{2\pi}\sin(4\pi D)\right)} \tag{18}$$

where $D \in [0, 0.5], C_q \in [C_{sx1}, {}^{C_{sx1}\cdot C_{sx2}}/_{C_{sx1}+C_{sx2}}]$.

From (18), the equivalent capacitance increases as the duty cycle changes from 0 to 0.5, indicating that the size of the V_g signal can be controlled directly to alter the equivalent capacitance, thereby achieving the desired compensation effect.

The equivalent capacitance was compensated through the control of the duty cycle of a switching tube to facilitate the charging and discharging of the capacitor, and the equivalent capacitance compensation technology could address the circuit mismatch issue and enhance the power and efficiency of the system.

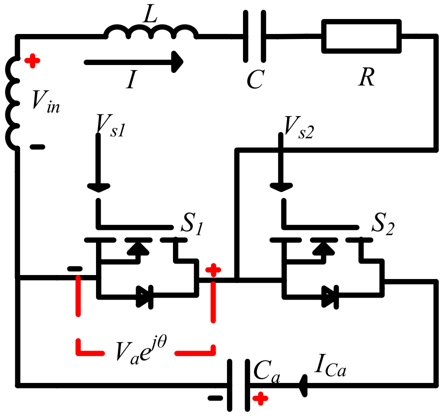

Fig. 16. Adaptive reactance compensation circuitry applied in the receiver.

B. Adaptive Reactance Compensation

Reactance caused by inductance, nonresistive reactance, and capacitance can be automatically eliminated using adaptive reactance compensation [28]. This is achieved by charging and discharging the capacitor at different times using two switching devices. As shown in Fig. 16, the detuning compensation circuit is realized on the receiver side of the LCC-S topology circuit.

The loop current I can be calculated as follows:

$$I = \frac{V_{\text{in}} - V_a e^{j\theta}}{R + j\left(\omega L - \frac{1}{\omega C}\right)} = \frac{V_{\text{in}} - V_a\cos\theta - jV_a\sin\theta}{R + j\left(\omega L - \frac{1}{\omega C}\right)} \tag{19}$$

where C is the compensation capacitance, L is the inductance of the receiver coil, R is the resistance of load, $V_a e^{j\theta}$ serves as compensating voltage to address the detuning compensation reactance phase, and θ is the phase difference.

The imaginary part of the current I^* can be calculated as follows:

$$I^* = \frac{\left(\omega L - \frac{1}{\omega C}\right)V_a\cos\theta - \left(\omega L - \frac{1}{\omega C}\right)V_{\text{in}} - V_a R\sin\theta}{R^2 + \left(\omega L - \frac{1}{\omega C}\right)^2}. \tag{20}$$

In order to compensate for detuning due to inductance variations, the imaginary part of the current I must be zero, and the

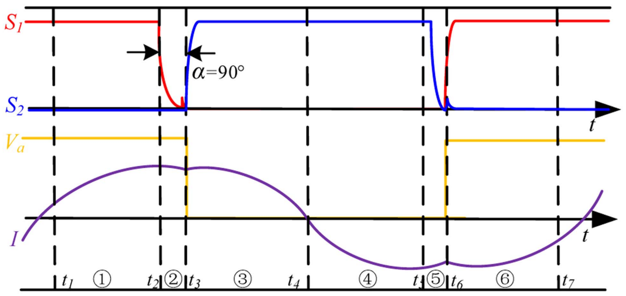

Fig. 17. Main waveforms of capacitive circuit compensation in six modes.

TABLE V
CIRCUIT ANALYSIS OF CAPACITOR CIRCUIT COMPENSATION

	S1	S2	*Va*	Status
①	ON	OFF	High	Charge
②	Deadtime	Deadtime	High	Charge
③	OFF	ON	Low	Charge
④	OFF	ON	Low	Discharge
⑤	Deadtime	Deadtime	Low	Discharge
⑥	ON	OFF	High	Discharge

compensation voltage $V_a e^{j\theta}$ depends on whether the circuit is inductive or capacitive. There are two cases of detuned circuits in Fig. 16, one in which detuning causes the circuit to appear inductive and the other in which detuning causes the circuit to appear capacitive.

The negative total impedance is produced when there is a decrease in inductance or an increase in capacitance, indicating the capacitive characteristics of the circuit. Conversely, the positive total impedance is produced when there is an increase in inductance or a decrease in capacitance, indicating the inductive characteristic of the circuit. The circuit simulation waveforms of the switching tube used for capacitive compensation are shown in Fig. 17 when the circuit exhibits capacitive characteristics. The control signal α is phase-shifted by 90° with respect to the input voltage. The circuit analysis for capacitor circuit compensation is shown in Table V.

MODE ①: During this interval, by hard-switching ON S_1 and hard-switching OFF S_2, the current increases and the capacitor charges. The voltage across the capacitor reaches a level equal to the compensating voltage V_a.

MODE ②: Both switches are OFF, and the capacitor is charged by the current *I* through the anti-parallel diodes.

MODE ③: The compensating voltage V_a is zero, and the current is allowed to flow through S_2.

MODE ④: The direction of current changes but it continues to flow through the switching device.

MODE ⑤: With both switches turned OFF, the current *I* is directed through the anti-parallel diodes connected to switch S_2. The compensating voltage is negative which is equal to the forward diode voltage drop.

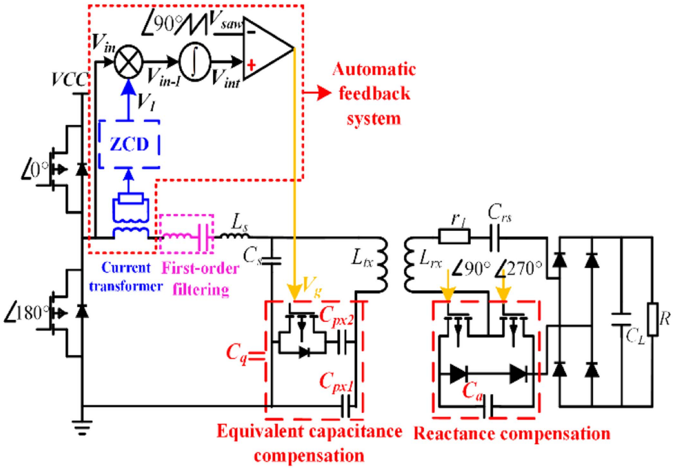

Fig. 18. Automatic resonance tuning based on LCC-S.

MODE ⑥: When switch S_1 is turned ON, the current flows through it, resulting in the discharge of capacitor C_a.

The analysis of the circuit in the inductive case follows a similar methodology as previously described. Based on this analysis, the utilization of the adaptive reactance compensation technique can effectively alleviate the detrimental effects caused by circuit mismatch, thereby resulting in enhanced system power and efficiency.

C. *Automatic Resonance Tuning Circuit*

In the context of the equivalent capacitance compensation technique, a singular switching tube is utilized to modulate the capacitor charging and discharging, effectively transforming it into an equivalent compensation capacitance. By adjusting the duty cycle of the switch tube, the capacitance value could be continuously adjusted, enabling soft switching of the tube and leading to a reduction in power consumption. However, the requirement for system feedback control to accommodate the varying duty cycles needed for different levels of inductance is a notable drawback.

Conversely, the adaptive reactance compensation method employs two switching tubes to regulate the reactance characteristics of distinct circuits using a fixed duty cycle control strategy. Remarkably, this method achieves adaptive control without the need for feedback mechanisms, streamlining the implementation process.

Utilizing a blend of the equivalent capacitance and adaptive reactance compensation techniques, an automatic resonance tuning system is implemented for detuning correction in the LCC-S circuit configuration.

In the autotuned resonance compensation system within the LCC-S topology, as illustrated in Fig. 18, the equivalent capacitance compensation technique is implemented on the transmitter side, while the receiver employs adaptive reactance compensation.

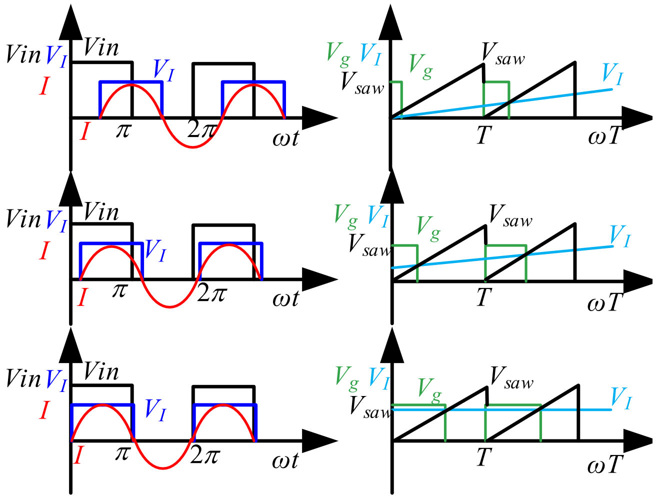

Fig. 19. Automatic resonance tuning system flow schematic. (a) Prior to the initiation of compensation. (b) During the ongoing process of compensation. (c) Upon completion of compensation.

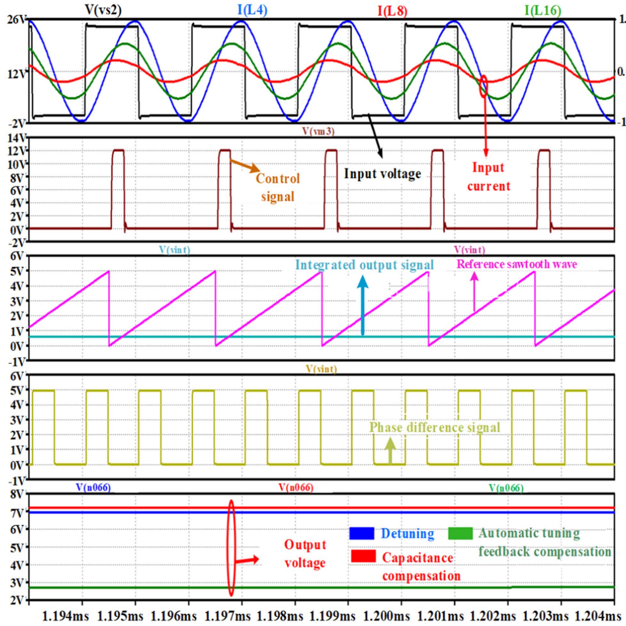

Fig. 20. Circuit waveform when compensation is not completed.

The transmitter comprises components such as the current transformer, over-zero detection circuit, phase comparator, integrator, reference sawtooth waveform generator, and comparator, collectively forming the automatic feedback system. This system facilitates the closed-loop regulation of equivalent capacitance compensation for detuning compensation on the transmitter. In parallel, the receiver employs adaptive reactance compensation to achieve detuning compensation. The automatic resonance tuning schematic diagram is shown in Fig. 19. Where V_{in} is the output voltage of the half-bridge circuit, I is the input current, V_I is the output voltage of the over-zero detection circuit, and the phase is consistent with the input current, V_{saw} is the reference sawtooth wave, V_{int} is the output voltage of the integrator, and V_g is the equivalent capacitance compensation of the switching tube control signal.

When the inductance of the transmitter coil decreases, the input impedance is inductive, so the input current phase lags behind the input voltage, and the phase difference is φ. At this time, the equivalent capacitance C_q is smaller than the capacitance to be compensated. After the phase comparator and the integrator, V_{int} gradually increases, and compared with the V_{saw}, the output V_g to control switching tube S_3, with the increase in the duty cycle of V_g, C_q is equal to the capacitance to be compensated, the input current and the phase of the input voltage coincide, and V_{int} also stops increasing. Completion of the closed-loop control of the transmitter detuning compensation.

D. Simulation Analysis of Autotuning Feedback Compensation

The schematic illustration of the autotuned feedback compensation system is designed using Ltspice simulation software, taking into account scenarios where variations occur in both the transmitting and receiving coils. Specifically, the inductance of transmitter inductance and receiver inductance are set at 3 μH each.

In Fig. 20, V_{in} represents the input voltage, I the input current, and V_{out} the output voltage, with these three parameters used as indicators for comparing three different cases. Through the waveforms in Fig. 20, it can be seen that when the inductance of the transmitter coil L_1 decreases, in the uncompensated state, the input current I experiences a phase lag with respect to the input voltage V_{in}, resulting in a phase difference between the two. In this initial stage, when C_q is smaller than the capacitance required to be compensated, the system has just commenced the compensation process, and a phase difference still exists between the input voltage and current. The amplitude of the integral output signal V_{int} is observed to be very small, resulting in a significantly lower duty cycle of the corresponding output control signal V_g. Consequently, the system output voltage has not yet reached the desired compensation state.

The detuning compensation process increases the duty cycle signal, increasing the equivalent capacitance to match the capacitance requiring compensation. The waveform of the circuit completed by detuning compensation is shown in Fig. 21. As can be seen from the figure, the input current and the input voltage are synchronized in phase after the compensation is completed, resulting in a phase difference of 0. The amplitude of the integrator output voltage V_{int} remains constant, and the duty cycle of the output control signal V_g remains constant. This indicates that the system is in a fully compensated state.

IV. EXPERIMENTAL ANALYSIS

A. Experimental Preparation

The simulations conducted in Section II reveal that when the folding angle of the coil changes from 180° to 90°, the variation in coil inductance is minimal, leading to only a slight deviation in system frequency. Consequently, with marginal inductance alterations, the detuning compensation impact remains modest. Conversely, within the folding range of 90° to 10°, the inductance of the coil can fluctuate significantly, causing

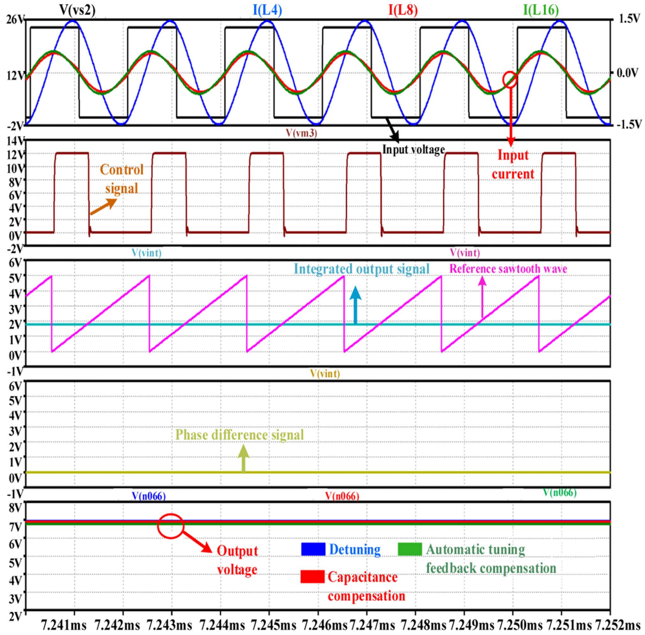

Fig. 21. Circuit waveform when compensation is completed.

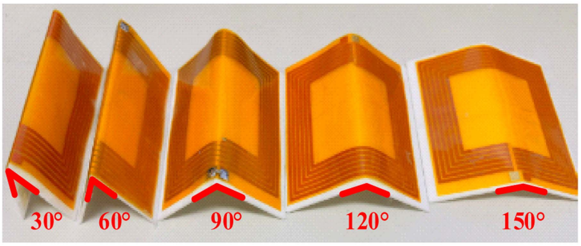

Fig. 22. Schematic diagram of the folded coil used in the experiment.

a noticeable frequency shift with substantial repercussions on the system. In such instances, the effectiveness of the designed compensation circuit can be more reliably evaluated. Therefore, this experiment focuses on the transmission characteristics under the flexible coil with different folding angles of 30°, 60°, 90°, 120°, and 150°. The schematic representation of the folded coil utilized in the experiment is depicted in Fig. 22.

To ensure minimal variation in coupling coefficients between the flexible coils at the transmitter and receiver across different folding angles, both coils are maintained in a folded state for experimentation. Additionally, the distance between the two coils affected the transmission characteristics of the system, and during the experiment, the distance between the two coils was kept unchanged to regulate the impact on the system's transmission characteristics.

To mitigate this influence, the distance is maintained unchanged to ensure that the two coils remain in a critical coupling state. When the system is strongly coupling region state, frequency splitting occurs, leading to the maximum output power point not aligning with the resonant frequency point. Even with detuned compensation, the system fails to achieve its optimal output. While the loosely coupling region state offers the highest efficiency and power at the resonance point, the efficiency and power are significantly reduced due to the long distance. Hence, the critical coupling state is selected as the experimental condition for this study, aiming to maintain an optimal balance between efficiency and power output.

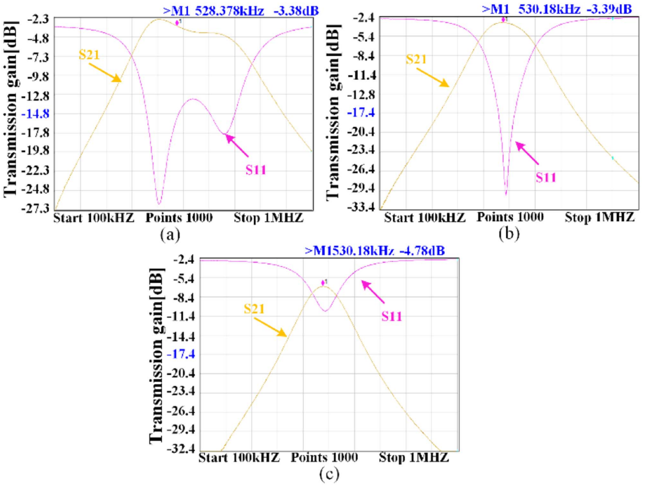

Fig. 23. (a) Strongly coupling region state. (b) Critical coupling. (c) Loosely coupling region state.

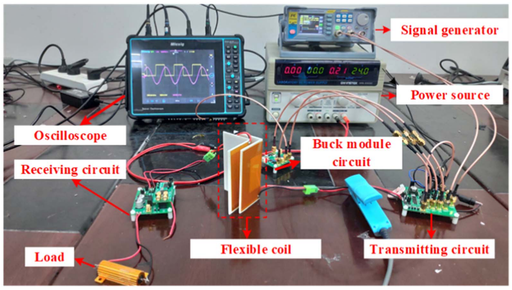

Fig. 24. System experimental setup.

Utilizing the vector network analyzer, the S21 and S11 waveform data of the transmitting and receiving coils are swept at varying distances to ascertain the critical coupling distance. The forward transmission coefficient of the receiving coil from the transmitting coil is represented by S21. The reverse transmission coefficient from the receiving end to the transmitting end is represented by S11. Port 1 is the inverter circuit output and port 2 is the rectifier circuit input at the receiving end. As shown in Fig. 23, critical coupling was achieved when the coils were positioned 30 mm apart at a folding angle of 90°, but reducing the coil separation below 30 mm resulted in the system entering an overcoupling state characterized by frequency splitting, while distances exceeding 30 mm led to an undercoupling state. To maintain the critical coupling condition, a separation distance of 30 mm between the coils is selected as the experimental parameter. Fig. 24 shows the overall experimental diagram of the automatic resonance tuning system, which corresponds to the system structure diagram in Fig. 18.

TABLE VI
PARAMETER LIST OF LCC-S TOPOLOGY OPERATING CONDITIONS

Symbol	Parameter	Value	Unit
V_{dc}	Input voltage	24	V
f	Inverter frequency	500	kHz
L_f	Filter inductors	17.56	μH
C_f	Filter capacitor	5.7	nF
L_s	Compensation inductors	2.3	μH
C_s	Compensation capacitor	44	nF
L_1	Transmitter coil inductance	4.56	μH
C_1	Transmitter compensation capacitance	4	nF
L_2	Receiver coil inductance	4.56	μH
C_2	Receiver compensation capacitance	22	nF
R	Load resistance	15	Ω
h	Distance between two coils	30	mm

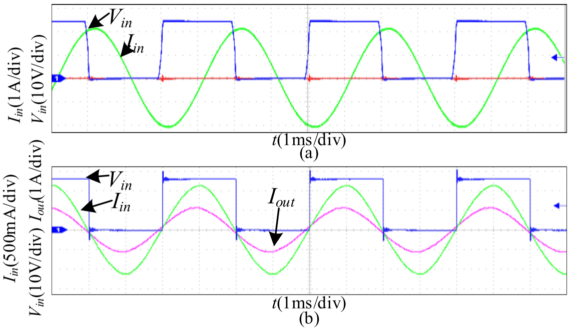

Fig. 25. (a) Waveforms of the system input voltage and transmitter coil current. (b) Waveforms of input and output of the current transformer and over-zero detection.

B. Experimental Result

The experiment is based on the LCC-S hybrid topology to satisfy the autotuning feedback compensation technology of the system. The operating conditions of the system are specified in Table VI. The autotuning compensation system of the LCC-S series topology is then analyzed experimentally using the parameters provided in Table VI.

Depending on the characteristics inherent to the LCC-S topology, the transmitter coil current maintains a constant value in the absence of consideration for the parasitic internal resistance. The waveforms of the system input voltage and transmitter current as shown in Fig. 25(a). According to (6), the peak transmitter coil current is calculated to be 2.11 A, whereas the actual measurement in the figure indicates a value of 2.08 A. Furthermore, the current phase lags 90° behind the input voltage phase.

The input current waveforms at the transmitter side captured by the input and output channels of the system current transformer, as well as the over-zero detection waveforms, are shown in Fig. 25(b). The current transformer, boasting a bandwidth of 1MHz, exhibits precise alignment with the current phase accuracy. Examination of the experimental waveforms reveals coherence between the input and output current phases, as well as synchronization between the phase of the output square wave from the over-zero detection and the current phase.

In accordance with the simulation results outlined in Section II, the variation in inductance of the receiving coil exerts a negligible influence on the system. Consequently, the experimentation in this work focused solely on five distinct folding angles of the transmitter coil. When the transmitter coil folds, its inductance diminishes, leading to an inductive impedance in the input circuit. This results in the input current lagging behind the input voltage, with automatic compensation aligning the current phase with the voltage phase.

The experimental waveforms of detuning and autocompensation for five folding angles (30°, 60°, 90°, 120°, and 150°) are shown in Fig. 26. When the transmitter coil is changed, resulting in reduced inductance, the input circuit displays inductive reactance, causing the input current to lag behind the input voltage. It demonstrates that when the system is in a detuned state at these angles, a phase difference between the input voltage and input current occurs.

The experimental simulation results depicted in Fig. 20 are confirmed in Fig. 26, demonstrating that an incomplete compensation leading to a phase difference in the system results in reduced system output power. Through modulation of the duty cycle of the switching tube, a continuous adjustment in the equivalent capacitance value enables automatic resonance compensation. Once the compensation process is finalized, the elimination of the phase difference signal facilitates the system to function in a resonant state, leading to an enhancement in output power. The experimental findings serve to corroborate the precision of the simulation outcomes depicted in Fig. 21. Moreover, the figure indicates that the 30° folding angle imposes the largest duty cycle, attributed to its maximum coil folding angle at this point in time. Conversely, the 150° folding angle yields the smallest duty cycle, as the folded coil is closest to the system plane, necessitating a smaller equivalent capacitance to achieve resonance. Compared to the 1 mW low-frequency power transfer reported in [40], the system in [41] is demonstrated to achieve 3.07 W of power transfer at 300 kHz, with an efficiency of 78%. Both systems are shown to utilize flexible coils for power transfer. In contrast, this article investigates the transmission characteristics under varying degrees of coil deformation. Power output of 2.5 W is maintained even with severe 30° misalignment. Furthermore, efficient power transmission is preserved after compensation, despite 180°–90° deviation scenarios.

The detuned waveforms shown in Figs. 26(g) and (i) correspond to coils folded at 150° and 120°, respectively, and it can be seen that there is a phase difference between the currents and voltages at this point, but the difference is small. This is due to the fact that in the range of 180° to 90°, the inductance of the coil varies less with the folding angle and the inductance decreases by only 10% from 180° to 90°, because the inductance change is small and the system frequency shift is also small. The experimental results further verify the correctness of the simulation results in Figs. 12 and 13. Table VII lists the supply voltages and supply currents for the input power of the system, and the output power is calculated by $P = U^2/R$.

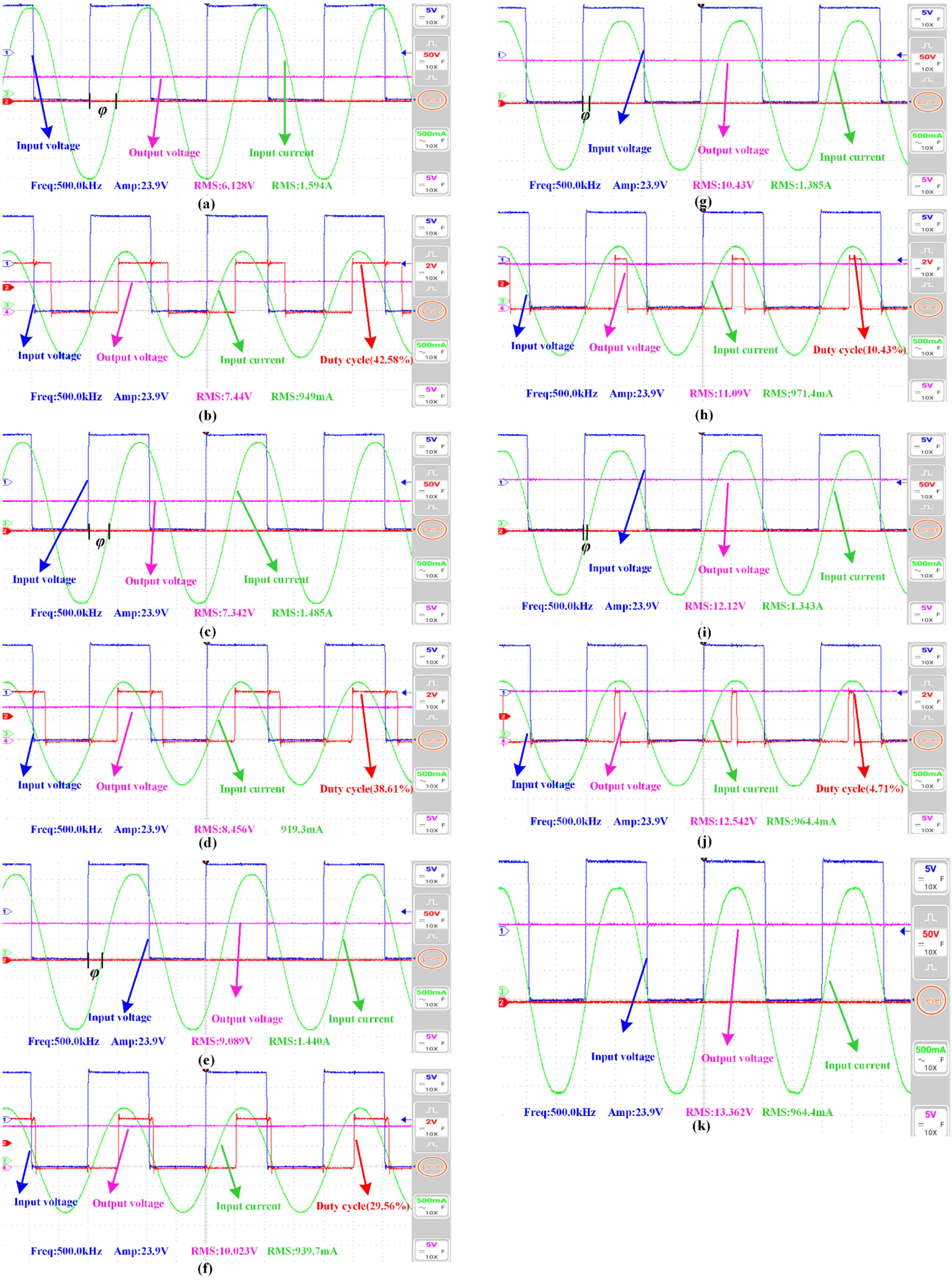

Fig. 26. Detuning and automatic resonance tuning under different folding angles. (a) Folded 30° uncompensated. (b) Folded 30° compensated. (c) Folded 60° compensated. (d) Folded 60° compensated. (e) Folded 90° uncompensated. (f) Folded 90° compensated. (g) Folded 120° uncompensated. (h) Folded 120° compensated. (i) Folded 150° uncompensated. (j) Folded 150° compensated. (k) Folded 180° in resonance.

TABLE VII
OUTPUT POWER AND TRANSMISSION EFFICIENCY FOR UNCOMPENSATED CONDITIONS WITH DIFFERENT FOLDING ANGLES

Folding angle	Supply Current	Output voltage	Output power	Input power	Efficiency
30˚	0.49 A	6.12 V	2.5 W	11.9 W	21%
60°	0.68 A	7.34 V	3.6 W	16.32 W	22%
90°	0.53 A	9.08 V	5.5 W	12.72 W	43%
120°	0.43 A	10.43 V	7.4 W	10.42 W	71%
150°	0.51A	12.12 V	9.8 W	12.41 W	79%
180	0.57 A	13.36 V	11.9 W	13.69 W	86%

TABLE VIII
OUTPUT POWER AND TRANSMISSION EFFICIENCY UNDER DIFFERENT FOLDING ANGLE COMPENSATION CONDITIONS

Folding angle	Supply Current	Output voltage	Output power	Input power	Efficiency
30˚	0.27 A	7.44 V	3.7 W	6.48 W	57%
60°	0.37 A	8.48 V	4.8 W	8.88 W	54%
90°	0.44 A	10.02 V	6.7 W	10.69 W	63%
120°	0.43 A	11.09 V	8.2 W	10.51 W	78%
150°	0.54 A	12.54 V	10.5 W	12.97 W	80%

In the detuned state, the output power decreased as the folding angle decreased, as the inductance of the flexible coil decreased with the smaller folding angle, leading to detuned amplification of the system and a resulting decline in the output power. Observation of the efficiency change can be clearly seen, the folding angle of 90°–180° when the system efficiency is reduced but the magnitude of the reduction is small, as shown in Fig. 10 folding 90°–180° range of the coil inductance change is small only about 10% change. But after 90° system efficiency changes significantly this is because the folding angle in 90° after the inductance reduction speed accelerated significantly, in 10° compared to the initial value of 55%, so its efficiency is greatly reduced.

Compared with the detuned state, the autotuning compensation at the same folding angle shows a slight enhancement of the output power, although this enhancement is not obvious, but it significantly improves the efficiency. Table VIII can be seen in 150°, 120° compensation after the efficiency changes are not obvious because the coil inductance change is small compensation effect is not obvious, observe 30°, 60°, 90° compensation after the three angles of the system efficiency is significantly improved, and the duty cycle with the folding angle decreases with increasing because the coil inductance continues to become smaller compensation capacitance increases the duty cycle increases, the overall results of the experiments. In general, the experimental results further verify the effectiveness of autotuning compensation.

V. CONCLUSION

Flexible coils are extensively utilized in wearable devices, foldable electronic products, and medical implants due to their distinctive characteristics. This article investigates the WPT flexible coil under magnetic coupling resonance and proposes a compensation method to address detuning issues caused by coil deformation. The analysis of detuned resonance in LCC-S topology circuits confirms that the reduction in coil inductance leads to a detuned state, diminishing transmission efficiency.

To alleviate detuning, an automatic feedback compensation system was established, implementing closed-loop control of the transmitter's equivalent capacitance compensation. The advantage of this design lies in its ability to restore the system to resonance through automatic tuning when detuning occurs due to flexible coil deformation, maintaining phase consistency without wireless communication, thus avoiding information loss from high-frequency switching and redundant algorithm control. The research results demonstrate that when the coil is in a flat state, the maximum output power reaches 13.69 W. However, as the folding angle is increased, the output power and transmission efficiency are observed to decrease. When the coil is folded from 180° to 90°, the frequency shift is found to be negligible due to the minor change in coil inductance, and the compensation effect is not pronounced. Nevertheless, at a 90° folding angle, the output power increases from 4 to 5 W, and the transmission efficiency improves from 43% to 62%. Furthermore, as the folding angle is decreased, the compensation effect becomes more evident. Compared to the detuned state, the automatic feedback compensation system's efficiency is demonstrated to be increased by at least 20% at folding angles of 30°, 60°, and 90°.

This article primarily investigated the system transmission characteristics of flexible coils under static deformation conditions. With the advancement of mobile wireless transmission technology, researching the characteristics of flexible coils under dynamic deformation conditions is of great significance. For instance, the volume and radiation of the equipment need to be considered under the high-speed rotation of rotating equipment. Additionally, the adverse effects of temperature rise and wear during the coil deformation in different application scenarios on the wireless energy transmission system should also be considered in future analysis.

REFERENCES

[1] D. Xu, Q. Zhang, and X. Li, "Implantable magnetic resonance wireless power transfer system based on 3D flexible coils," *Sustainability*, vol. 12, no. 10, May 2020, Art. no. 4149.

[2] X. Mou, D. Gladwin, J. Jiang, K. Li, and Z. Yang, "Near-field wireless power transfer technology for unmanned aerial vehicles: A systematical review," *IEEE J. Emerg. Sel. Top. Ind. Electron.*, vol. 4, no. 1, pp. 147–158, Jan. 2023.

[3] C. Qi, N. Sugita, and T. Shinshi, "Development of a flexible coil based on conductive polymer composite for PDMS-based soft electromagnetic microactuators," *Sens. Actuators A, Phys.*, vol. 363, Dec. 2023, Art. no. 114766.

[4] C. Mandache, R. Desnoyers, and Y. Bombardier, "Crack growth monitoring with structure-bonded thin and flexible coils," *Sensors*, vol. 22, no. 24, Dec. 2022, Art. no. 9958.

[5] Y. Yao et al., "A flexible thin-film inductor for high-efficiency wireless power transfer," *IEEE Electron Device Lett.*, vol. 44, no. 3, pp. 504–507, Mar. 2023.

[6] J.-Q. Zhu, Y.-L. Ban, R.-M. Xu, and C. C. Mi, "An NFC-connected coupler using IPT-CPT-combined wireless charging for metal-cover smartphone applications," *IEEE Trans. Power Electron.*, vol. 36, no. 6, pp. 6323–6338, Jun. 2021.

[7] B. Garnier, P. Mariage, F. Rault, C. Cochrane, and V. Koncar, "Textile dual-band NFC-A4WP (13.56–6.78 MHz) combiner for wireless energy and data transmission for connected clothing," *Sci. Rep.*, vol. 13, no. 1, Apr. 2023, Art. no. 5613.

[8] J. Lee, B. Bae, B. Kim, J. Lim, and B. Lee, "A load-independent battery charging system for multiple wearable devices using conductive textile," *IEEE Trans. Ind. Electron.*, vol. 71, no. 11, pp. 15211–15215, Nov. 2024.

[9] P. Escobedo, A. Pousibet-Garrido, N. Lopez-Ruiz, M. A. Carvajal, A. J. Palma, and A. Martinez-Olmos, "Bed-based ballistocardiography system using flexible RFID sensors for noninvasive single- and dual-subject vital signs monitoring," *IEEE Trans. Instrum. Meas.*, vol. 73, pp. 1–12, Feb. 2024, Art. no. 2002912.

[10] S. Cetin and Y. E. Demirci, "High-efficiency LC-S compensated wireless power transfer charging converter for implantable pacemakers," *Int. J. Circuit Theory Appl.*, vol. 50, no. 1, pp. 122–134, Jan. 2022.

[11] A. P. M. Raj, T. Stalin, and P. V. Y. Alvarado, "Flexible fiber inductive coils for soft robots and wearable devices," *IEEE Robot. Automat. Lett.*, vol. 7, no. 2, pp. 5711–5718, Apr. 2022.

[12] F. Fusco, V. U. Castrillo, H. M. R. Giannetta, M. Albano, and E. Cavallini, "Methods, standards and components for wireless communications and power transfer aimed at intra-vehicular applications of launchers," *Aerospace*, vol. 11, no. 2, Feb. 2024, Art. no. 132.

[13] E. Z. Y. Hou, "Performance optimization of harmonized flexible printed coils of axial magnetized magnetostrictive patch transducers for pipeline inspection," *Measurement*, vol. 199, Aug. 2022, Art. no. 111478.

[14] D. Vital, P. Gaire, S. Bhardwaj, and J. L. Volakis, "An ergonomic wireless charging system for integration with daily life activities," *IEEE Trans. Microw. Theory Techn.*, vol. 69, no. 1, pp. 947–954, Jan. 2021.

[15] H. T. Nguyen et al., "Review map of comparative designs for wireless high-power transfer systems in EV applications: Maximum efficiency, ZPA, and CC/CV modes at fixed resonance frequency independent from coupling coefficient," *IEEE Trans. Power Electron.*, vol. 37, no. 4, pp. 4857–4876, Apr. 2022.

[16] Y. Zhang et al., "A hybrid compensation topology with constant current and constant voltage outputs for wireless charging system," *IEEE Trans. Transp. Electrific.*, vol. 9, no. 2, pp. 2070–2080, Jun. 2023.

[17] H. Chen, D. Qiu, C. Rong, and B. Zhang, "A double-transmitting coil wireless power transfer system based on parity time symmetry principle," *IEEE Trans. Power Electron.*, vol. 38, no. 11, pp. 13396–13404, Nov. 2023.

[18] Y. Guan, C. Liu, Y. Wang, W. Wang, and D. Xu, "Analysis and design of a high-frequency low-profile converter for bendable equipment," *IEEE Trans. Power Electron.*, vol. 36, no. 11, pp. 12834–12842, Nov. 2021.

[19] S. Jeong et al., "Analysis of repetitive bending on flexible wireless power transfer (WPT) PCB coils for flexible wearable devices," *IEEE Trans. Compon., Packag. Manuf. Technol.*, vol. 12, no. 11, pp. 1748–1756, Nov. 2022.

[20] R. Zhang et al., "Self-tuning WPT system with constant voltage output under resonance frequency shift," *IEEE Trans. Power Electron.*, vol. 39, no. 1, pp. 1713–1722, Jan. 2024.

[21] W. Li, Q. Zhang, C. Cui, and G. Wei, "A self-tuning S/S compensation WPT system without parameter recognition," *IEEE Trans. Ind. Electron.*, vol. 69, no. 7, pp. 6741–6750, Jul. 2022.

[22] J. Li, S. Yu, N. Kou, Z. Ding, and Z. Zhang, "Cylindrical magnetically coupled resonant wireless power transfer system based on flexible PCB coils," *IEEE Microw. Wireless Compon. Lett.*, vol. 32, no. 12, pp. 1479–1482, Dec. 2022.

[23] W. Xiong et al., "A dual-frequency-detuning method for improving the coupling tolerance of wireless power transfer," *IEEE Trans. Power Electron.*, vol. 38, no. 6, pp. 6923–6928, Jun. 2023.

[24] L. Yang et al., "Single wire capacitive wireless power transfer system for wearable biomedical sensors based on flexible graphene film material," *IEEE Trans. Biomed. Circuits Syst.*, vol. 16, no. 6, pp. 1337–1347, Dec. 2022.

[25] M. Wagih, A. Komolafe, I. Ullah, A. S. Weddell, and S. Beeby, "A wearable all-printed textile-based 6.78 MHz 15 W-output wireless power transfer system and its screen-printed joule heater application," *IEEE Trans. Ind. Electron.*, vol. 71, no. 4, pp. 3741–3750, Apr. 2024.

[26] I. A. Shah, M. Zada, S. A. A. Shah, A. Basir, and H. Yoo, "Flexible metasurface-coupled efficient wireless power transfer system for implantable devices," *IEEE Trans. Microw. Theory Techn.*, vol. 72, no. 4, pp. 2534–2547, Apr. 2024.

[27] D. Kar, B. George, and K. Sridharan, "Design and implementation of a magnetic coupling based segmented bend angle sensor for a soft robotic gripper," *IEEE Trans. Instrum. Meas.*, vol. 73, pp. 1–10, Mar. 2024, Art. no. 9505610.

[28] L. Shi, P. Alou, J. Á. Oliver, J. C. Rodriguez, A. Delgado, and J. A. Cobos, "A self-adaptive wireless power transfer system to cancel the reactance," *IEEE Trans. Ind. Electron.*, vol. 68, no. 12, pp. 12141–12151, Dec. 2021.

[29] Y. Yang, "A passive augmented circuit for EMI reductions of full-bridge inverters with conventional phase shift control in wireless power transfer systems," *IEEE Trans. Power Electron.*, vol. 38, no. 11, pp. 13286–13297, Nov. 2023.

[30] G. Zhu, J. Dong, F. Grazian, and P. Bauer, "A parameter recognition-based impedance tuning method for SS-compensated wireless power transfer systems," *IEEE Trans. Power Electron.*, vol. 38, no. 11, pp. 13298–13314, Nov. 2023.

[31] D. Guo, Y. Su, H. Yin, H. Lan, and D. Li, "Self-adaptive resonance technology for wireless power transfer systems to eliminate impedance mismatches," *IEEE Trans. Power Electron.*, vol. 39, no. 8, pp. 10482–10495, Aug. 2024.

[32] S. A. Chowdhury, S. Kim, S. Kim, J. Moon, I. Cho, and D. Ahn, "Automatic tuning resonant capacitor to fix the bidirectional detuning with ZVS in wireless power transfer," *IEEE Trans. Ind. Electron.*, vol. 71, no. 6, pp. 5683–5692, Jun. 2024.

[33] S. Ali Khan and D. Ahn, "Automatic resonance tuning with ON/OFF soft switching for push-pull parallel-resonant inverter in wireless power transfer," *IEEE Trans. Power Electron.*, vol. 37, no. 9, pp. 10133–10138, Sep. 2022.

[34] P. Yadav and M. Veerachary, "Auxiliary coil based square coupler for wireless power transfer system," *IEEE Trans. Ind. Appl.*, vol. 58, no. 4, pp. 4980–4993, Jul./Aug. 2022.

[35] J. Li, X. Zhang, and X. Tong, "Research and design of misalignment-tolerant LCC–LCC compensated IPT system with constant-current and constant-voltage output," *IEEE Trans. Power Electron.*, vol. 38, no. 1, pp. 1301–1313, Jan. 2023.

[36] X. Wang, J. Xu, H. Ma, and P. Yang, "A high efficiency LCC-S compensated WPT system with dual decoupled receive coils and cascaded PWM regulator," *IEEE Trans. Circuits Syst. II, Exp. Briefs*, vol. 67, no. 12, pp. 3142–3146, Dec. 2020.

[37] R. Chirila, A. S. Dahiya, C. Urlea, P. Schyns, and R. Dahiya, "3-D printed microfluidic coils with liquid metal for wireless motion sensing," *IEEE Sens. Lett.*, vol. 7, no. 6, Jun. 2023, Art. no. 2501504.

[38] A. Narvaez, C. Carretero, I. Lope, and J. Acero, "Printed circuit board coils of multitrack litz structure for 3.3-kW inductive power transfer system," *IEEE Trans. Transp. Electrific.*, vol. 9, no. 3, pp. 3947–3957, Sep. 2023.

[39] Z. Yuan, M. Saeedifard, C. Cai, Q. Yang, P. Zhang, and H. Lin, "A misalignment tolerant design for a dual-coupled LCC-S-compensated WPT system with load-independent CC output," *IEEE Trans. Power Electron.*, vol. 37, no. 6, pp. 7480–7492, Jun. 2022.

[40] K. Sondhi et al., "Flexible screen-printed coils for wireless power transfer using low-frequency magnetic fields," *J. Micromech. Microeng.*, vol. 29, no. 8, Jun. 2019, Art. no. 084006.

[41] C. Xiao, D. Cheng, and K. Wei, "An LCC-C compensated wireless charging system for implantable cardiac pacemakers: Theory, experiment, and safety evaluation," *IEEE Trans. Power Electron.*, vol. 33, no. 6, pp. 4894–4905, Jun. 2018.

Guoyuan Cen was born in Fangchenggang, China, in 1999. He received the bachelor's degree in Electrical engineering and automation from the Guilin University of Electronic Science and Technology, Guilin, China, in 2022. He is currently working toward the master's degree in power electronics and power transmission in the Chengdu University of Electronic Science and Technology in China, Chengdu, China.

His current research interests include wireless power transmission energy transmission, power electronics and their applications, and automation of power systems.

Congling Wang received the B.S. degree in aircraft engine design engineering from the Nanjing University of Aeronautics and Astronautics, Nanjing, China, in 1991, and the M.S. degree in mechanical engineering from the University of Electronic Science and Technology of China (UESTC), Chengdu, China, in 1996.

Since 1996, he has been a Faculty Member with the School of Mechatronics Engineering. He is currently an Associate Professor with UESTC. He has taught many courses, such as "power supply technology," "power electronic converter technology," "circuit analysis," etc. His research interests include mechatronics engineering, electrical engineering, and automation.

Ping Yang received the B.S. degree in mechanical engineering from the Shanghai Jiao Tong University, Shanghai, China, in 1984, and the M.S. degree in mechanical engineering from Sichuan University, Chengdu, China, in 1987.

He was visiting Victory University, Australia, in 2004, and was a Visiting Scholar with the S. M. Wu Manufacturing Research Center, University of Michigan, Ann Arbor, MI, USA, from 2009 to 2010, and was visiting the University of California at Irvine, Irvine, USA, in 2012. He is currently a Full Professor with the School of Mechatronics Engineering, University of Electronic Science and Technology of China (UESTC), Chengdu, China. He is also the Dean of the School of Mechanical and Electrical Engineering, UESTC. He has authored more than 60 articles in various journals and international conferences, and several books on mechatronics and instrumentation. His research interests includes mechatronics engineering, electrical engineering and automation, computer-aided control and instrumentation, smart mechatronics, and detection and automation of mechan-ical equipment.

Dr. Yang was the recipient of several provincial awards for his contribution in teaching and academic research.

Amr S. Zalhaf was born in Tanta, Egypt, in 1988. He received the B.Sc. and M.Sc. degrees in electrical engineering from Tanta University, Tanta, Egypt, in 2010 and 2014, respectively, and the Ph.D. degree in energy resources engineering from the Egypt-Japan University of Science and Technology, Alexandria, Egypt, in 2019.

Since 2010, he has been with the Faculty of Engineering, Tanta University, where has been an Assistant Professor since 2019. He was a Visiting Scholar with the Department of Electrical and Electronic Engineering, School of Engineering, Tokyo Institute of Technology, Tokyo, Japan, in 2018. He is currently a Postdoctoral Fellow with the School of Mechanical and Electrical Engineering, University of Electronic Science and Technology of China, Chengdu, China. He was a Visiting Scholar with the Department of Electrical and Electronic Engineering, School of Engineering, Tokyo Institute of Technology, in 2018. He authored or coauthored more than 40 papers in international journals and conferences in addition to some papers accepted and under review. His research interests include lightning protection, wind energy, PV systems, smart grids, Internet of Things, and load side management.

Yang Han (Senior Member, IEEE) received the Ph.D. degree in electrical engineering from Shanghai Jiaotong University, Shanghai, China, in 2010.

In 2010, he joined the University of Electronic Science and Technology of China (UESTC), Chengdu, China, where he has been an Associate Professor in 2013 and a Full Professor in 2021. From 2014 to 2015, he was a Visiting Scholar with the Department of Energy Technology, Aalborg University, Aalborg, Denmark. He is currently with the School of Mechanical and Electrical Engineering, UESTC. He has received several national and provincial projects, and more than 30 industrial projects in the area of power electronics, smart grid, microgrid, and power quality analysis and compensation. He holds more than 40 issued and pending patents. He has authored a book *Modeling and Control of Power Electronic Converters for Microgrid Applications* (Springer). His research interests include the ac/dc micro-grids, active distribution networks, power quality, grid-connected converters for renewable energy systems, active power filters, multilevel converters, and static synchronous compensators.

Dr. Han was listed as "World's Top 2% Scientist" by Stanford University in 2022, and Highly Cited Chinese Researcher by Elsevier in 2023, and was the recipient of the Young Scientist Award in CPESE 2021, the Provincial Science and Technology Award in 2020 and 2022, the Science and Technology Award from Sichuan Electric Power Company in 2019, the Academic Talent Award by UESTC, in 2017, the Baekhyun Award by the Korean Institute of Power Electronics, in 2016. He served as an Associate Editor of *Journal of Power Electronics* and IEEE ACCESS (2019–2020).